Nanoscale

Molecular Tunnel Junctions Based on Mixed SAMs: Exponential Correlation of the Average Metal-HOMO Coupling with SAM/Metal Work Function

Journal:	*Nanoscale*
Manuscript ID	NR-ART-02-2025-000487.R1
Article Type:	Paper
Date Submitted by the Author:	09-Mar-2025
Complete List of Authors:	Jeong, Gookyeong; University of Minnesota, Department of Chemical Engineering and Materials Science Frisbie, C.; University of Minnesota, Department of Chemical Engineering and Materials Science

Molecular Tunnel Junctions Based on Mixed SAMs: Exponential Correlation of the Average Metal-HOMO Coupling with SAM/Metal Work Function

Gookyeong Jeong and C. Daniel Frisbie*

Department of Chemical Engineering and Materials Science, University of Minnesota, Minneapolis, Minnesota 55455, United States

*E-mail: frisbie@umn.edu

Abstract

We report the transport characteristics of molecular tunnel junctions based on binary mixed self-assembled monolayers (SAMs) of aromatic molecules using the conducting probe atomic force microscopy platform. The molecules include terphenyl dithiol and two derivatives, 2′,3′,5′,6′-tetrafluoroterphenyl dithiol and 4,4'-(bicyclo[2.2.2]octane-1,4-diyl)dibenzenethiol, whose junction conductances differ from terphenyl dithiol by factors of 10 and 100, respectively. The junction conductance G varies exponentially with binary SAM composition, not linearly, as might be expected. By employing an analytical model for the off-resonant current-voltage (I-V) behavior, we extract the electronic density of states parameters for junctions with Au tip and substrate contacts as a function of binary SAM composition. The average HOMO to Fermi level offset ε_h is weakly dependent on SAM composition, reflecting commonly observed HOMO level pinning. In stark contrast, and in correspondence with the conductance results, the average metal-HOMO coupling Γ depends exponentially on composition, not linearly as simple composition-based averaging predicts. On the other hand, Kelvin probe measurements of binary mixed SAM-metal work functions reveal that work function (or work function change $\Delta\Phi$) varies linearly with SAM composition; it is a simple sum of the single component SAM work functions weighted by their relative surface coverages. Thus, G and Γ are both exponentially correlated with $\Delta\Phi$; variation of $\Delta\Phi$ by 360 meV (~7%) tunes G by >100x and Γ by a factor of 10, with smaller work functions (and larger $\Delta\Phi$ values) leading to larger G and Γ values. Qualitatively, a correlation between Γ and $\Delta\Phi$, which both reflect interfacial charge transfer, appears reasonable, but a fundamental understanding requires a first principles model that can also account for the simultaneous pinning of ε_h.

Introduction

Understanding the relationships between molecular structure, orbital energies, orbital localization, metal-orbital coupling, and measured current-voltage (*I-V*) behavior in molecular tunnel junctions (MTJs) is a difficult and central challenge in molecular electronics.[1–23] A key link between structure and transport is the junction electronic density of states (DOS) because its two important metrics, namely the frontier orbital energy offset from the Fermi level ε and the metal-orbital coupling Γ, Figure 1, are critical to electronic transmission.[24–38] Analysis of junction *I-V* behavior focuses on extracting these metrics as a function of junction structure. We and others have shown that these quantitative parameters can be determined from *I-V* data using analytical models and tabulated as a function of molecular architecture, metal-molecule bonding, and choice of contact metals, for example.[39–47]

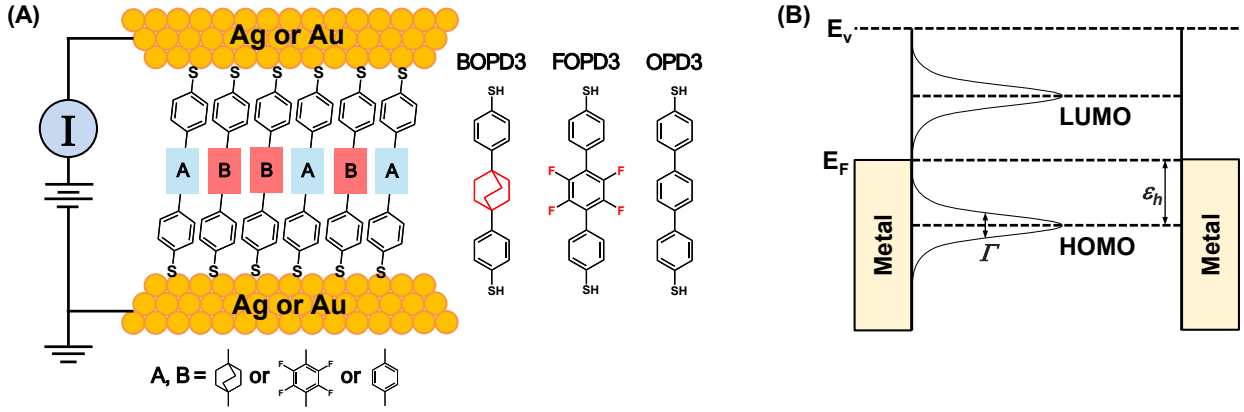

Figure 1. SAM-based molecular tunnel junctions. (A) Scheme of CP-AFM molecular junctions based on SAMs and structures of key molecules. Single component SAMs and mixtures of the BOPD3, FOPD3 and OPD3 molecules were examined using Ag or Au contacts as shown. (B) General electronic structure of single component molecular tunnel junctions indicating the two principal metrics, the HOMO offset energy ε_h and the metal-HOMO coupling Γ.

Many molecular junctions are based not on single molecules, but rather on self-assembled monolayers (SAMs) such that tens to millions of molecules contribute to the electronic transport, depending on the particular testbed. A natural question to ask then is, what is the role of intermolecular interactions on the measured transport and the junction DOS parameters? It turns

out that this is quite tricky to answer as current analytical models for MTJs do not include a parameter to account for the broadening of the DOS due to intermolecular interactions; the Γ parameter is explicitly for metal-orbital coupling. Recently, this problem has been considered theoretically, and comparison with experiments will be forthcoming.[48]

Rather than ask explicitly about the role of intermolecular interactions, we can change the question posed above to: What is the role of *SAM composition* on the measured transport and electronic structure? This question turns out to be more readily answerable. In an initial attempt to address it we have used the conducting probe atomic force microscopy (CP-AFM) platform to measure junction transport through mixed SAMs of alkyl (CnT) and fluoroalkyl (F-CnT) thiols, where n refers to the number of carbons in the chain.[49] That study revealed that a primary effect of making mixed CnT_x:F-$CnT_{(1-x)}$ SAMs was that the metal-SAM work function varied linearly with fractional composition x. Junction conductance on the other hand depended exponentially on composition and therefore by combining the two results we could demonstrate that conductance was exponentially correlated with work function. This correlation was qualitatively understandable as strong dependence of junction conductance on metal work function (Ag vs Au vs Pt) has been widely reported for single component SAMs.[39,41,50,51] If making *mixed* SAMs systematically tunes the work function, then one can anticipate that varying the composition of a SAM binary mixture will also tune conductance.

In terms of the *average* junction DOS, however, one could wonder whether the mixed SAM composition impacts average ε or Γ, and by how much? This question was not addressed in our prior study.[49] Here we address it using mixed SAMs of aromatic molecules 4,4'-(bicyclo[2.2.2]octane-1,4-diyl)dibenzenethiol (BOPD3), 2′,3′,5′,6′-tetrafluoroterphenyl dithiol (FOPD3), and terphenyl dithiol (OPD3) shown in Figure 1. In contrast to OPD3, which has been

extensively characterized in MTJs,[37,39,52–54] molecules BOPD3 and FOPD3 have not been reported before in SAMs or molecular junctions, as far as we are aware. There were two primary considerations in designing BOPD3 and FOPD3. First, we wanted the conductances of these two molecules to be significantly different from each other and from OPD3 so that a broad range of conductances would be observed in binary mixed SAM experiments, as will be made clearer below. Second, we needed a convenient method to determine the mole fraction of each type of molecule in binary SAMs. The F-atom labeling of FOPD3 provided a solution as F_{1s} core electrons are easily observable by X-ray photoelectron spectroscopy (XPS).

Thus, part of our report here concerns characterization of BOPD3 and FOPD3 single component SAMs and analysis of their conductance behavior in CP-AFM junctions with Au and Ag contacts. We demonstrate that insertion of the saturated bicyclo[2.2.2]octyl group between phenyl rings in BOPD3 decreases its conductance substantially (by more than two orders of magnitude) compared to OPD3, as expected. Likewise, fluorination of the middle ring in FOPD3 also turns out to lower its conductance compared to OPD3, though not as much as BOPD3; its conductance is intermediate. Further, we show that for single component SAMs of BOPD3 and FOPD3 the *I-V* characteristics are well described with an off-resonance single level tunneling model (orSLM),[37,39,43,44] and thus we can readily extract the electronic structure parameters ε and Γ. The metal dependence (Ag vs Au) of the transport characteristics and ultraviolet photoelectron spectroscopy (UPS) measurements confirm that the HOMO, not the LUMO, is the facilitating orbital for all junctions studied here.

We proceed to make $FOPD3_x$:$BOPD3_{(1-x)}$ and $FOPD3_x$:$OPD3_{(1-x)}$ binary SAM mixtures, taking advantage of the distinct F_{1s} XPS peak of FOPD3 to estimate relative coverage x, as noted above. In tunneling measurements on both SAM mixtures, we find that low bias conductance *G*

has exponential dependence on SAM composition, similar to our prior results on aliphatic SAMs,[49] but now extended to pi-conjugated systems. Conductance of the mixed SAMs is thus not the simple average of the single component molecular conductances weighted by their relative surface coverages, as one might expect; rather, conductance has exponential dependence on composition. In contrast, we observe by Kelvin probe measurements that the mixed SAM work functions are indeed linearly dependent on composition. We thus demonstrate that G is exponentially correlated with SAM work function, again consistent with our prior report.[49] Importantly, we use the orSLM analysis to discover that the sensitivity of G to work function derives from strong changes in average metal-HOMO coupling Γ, not from changes in average HOMO energy offset ε_h. In fact, average ε_h^{mix} for the mixed SAMs is almost independent of SAM composition and work function, while Γ^{mix} exhibits exponential dependence. Thus, our collective results not only reinforce our initial report,[49] but they extend it to a different molecular system and reveal strongly contrasting behavior for Γ^{mix} and ε_h^{mix} as a function of SAM composition and work function.

In general, our work here on both the single component and mixed SAMs of OPD3, BOPD3, and FOPD3 underscores the importance of two factors that impact Γ, namely molecular architecture and metal-SAM work function. Prior work has also shown clearly that molecular length and metal-molecule contact chemistry critically impact Γ.[39,43,44] Thus Γ subsumes at least four inter-related structural and electronic factors in molecular junctions: bonding architecture, molecular length, metal-molecule contacts, and metal-SAM work function. Understanding this thoroughly requires a microscopic model of molecular junction transport that can also account for the pronounced pinning of ε_h.[37,42,43] We believe the data and initial analysis provided here and elsewhere[37,41–44] can serve as useful reference points for theoretical investigations.

Experimental Section

Materials. Au nuggets (99.999%) were purchased from Mowrey, Inc. (St. Paul, MN). Evaporation boats and Cr rods were purchased from R. D. Mathis (Long Beach, CA). SiO_2/Si wafers were purchased from Silicon Valley Microelectronics, Inc. (Santa Clara, CA). Contact mode AFM tips (DNP-10) were purchased from Bruker AFM Probes. All chemicals and solvents were purchased from Sigma Aldrich or ThermoFisher Scientific and used as received.

Synthesis. The synthesis and characterization of the terphenyl dithiol (OPD3), 2′,3′,5′,6′-tetrafluoroterphenyl dithiol (FOPD3), and 4,4'-(bicyclo[2.2.2]octane-1,4-diyl)dibenzenethiol (BOPD3) are described in Supporting Information.

Preparation of Template-stripped Metal Substrates and Metal-coated Tips. Ultra flat template-stripped metal substrates ($metal^{TS}$) were prepared following previous protocols.[55–57] For Au^{TS} or Ag^{TS} substrates, 5000 Å of metal was deposited onto a SiO_2 wafer by e-beam evaporation without an adhesion layer. Small Si chips (1 cm^2) were glued with an epoxy product (EPOTEK-353 ND, Epoxy Technologies, MA) onto the metal substrates, and the epoxy layer was cured in an oven at 80˚C for 3 h. The Si-backed $metal^{TS}$ substrate was cleaved by hand from the substrate wafer, and immediately immersed into a deposition solution to grow SAMs. For metal-coated tips, 500 Å of Au or Ag metal on top of a 50 Å Cr adhesion layer (0.1 Å/s) was evaporated at a rate of 0.6 Å/s onto AFM tips using a home-built thermal evaporator in a N_2-filled glove box. AFM tips were transferred with minimal air exposure to another glove box where the CP-AFM was installed.

SAM Formation. Pure or mixed SAMs of the OPD3, FOPD3, and BOPD3 precursors were formed from anhydrous tetrahydrofuran (THF) solutions. In all cases the total concentration of target molecules in the deposition solutions was 0.5 mM. To make mixed SAMs the ratios of the

two components were varied ensuring that the total molecular concentration was 0.5 mM. Following dissolution of the appropriate solids, THF solutions were purged with N_2 from a balloon through a needle for 20 min, and subsequently 50 μL of 1.0 M tetrabutylammonium fluoride (TBAF) deprotecting agent in THF was added (20 equiv.) to the solution. Ag^{TS} or Au^{TS} substrates were then immersed immediately in the solution under N_2 for 24 h in the dark. Afterwards, SAM-coated substrates were taken out of solution, washed with THF and then absolute ethanol, dried with N_2, and used immediately for each measurement.

Characterization of SAMs. A Versa Probe III XPS system (Physical Electronics, Inc) with a monochromatized Al Kα X-ray source (1486.6 eV) and a 5.0 x 10^{-8} Pa base pressure was employed to characterize each SAM. Samples were mounted on the sample holder using double-sided carbon tape. Typical high resolution acquisition parameters were: 100 μm X-ray spot diameter, 25 W, 15 kV X-ray source power, 55 eV analyzer pass energy, 20 ms dwell time per step, 0.05 eV/step, and a 45˚ analyzer take-off angle. $Au4f_{7/2}$ or $Ag3d_{5/2}$ binding energies at 84.0 eV and 368.2 eV, respectively, were used as reference peaks.

Angle-resolved XPS (ARXPS) with take-off angles of 30˚, 40˚, 50˚, 60˚, and 70˚ was completed using the same instrument in order to characterize SAM thickness and molecular tilt angle on Au^{TS}. Variable angle spectroscopic ellipsometry (J. A. Woollam Co., Inc.) was also employed as an additional thickness measurement for SAMs on Au^{TS} substrates. Spectral range was 600-900 nm with steps of 15 nm at 3 different incident angles (60˚, 70˚ and 80˚). The index of refraction, *n*, and the absorption coefficient, *k*, were taken to be 1.45 and 0, respectively.[58,59] The ellipsometry analysis gave thicknesses for BOPD3 and FOPD3 of 1.47±0.09 nm and

1.58±0.02 nm, respectively, and molecular tilt angles of 33.9˚ and 25.8˚, respectively, on Au^{TS}, which were similar to the ARXPS results shown in Supporting Information.

The Fermi level to HOMO offsets, ε_h, of pure and mixed SAMs on Ag^{TS} and Au^{TS} were also characterized by UPS using the same Versa Probe III instrument used for XPS. A He I light source (21.2 eV) was employed with analyzer settings of 1.3 eV pass energy, 0.05 eV/step, 20 s dwell time per step, and 45° take-off angle. Spectra were referenced to the Fermi level.

The work functions of pure and mixed SAMs on Ag^{TS} and Au^{TS} were measured using a conventional Kelvin probe (SKP5050, KP Technology) at room temperature and ambient pressure in the dark. SAMs were mounted and grounded to the Kelvin probe stage and a 2 mm diameter probe tip was brought close (<~1 mm) to the sample. The surfaces of the samples were scanned by the tip and the work functions at the different locations were collected and averaged. The measured work functions were referenced to the value of 1-hexadecanethiol SAMs on Au whose work function was measured in a previous study (4.3 eV).[60]

Junction *I-V* measurements. The transport behavior of tunnel junctions based on pure and mixed SAMs on Ag^{TS} and Au^{TS} were examined using CP-AFM with Ag and Au coated tips, respectively, in a Ar-filled glove box (MBraun) in which the O_2 level was maintained at less than 4.0 ppm. Metal coated AFM tips contacted individual SAMs with a compressive load of ~ 1 nN. The sample was grounded, and voltage was applied to the tip using a Keithley 236 source measure unit that also recorded the current. The plotted curves correspond to a sweep from negative to positive voltage. For higher bias measurements the tip potential was swept between ± 1.0 V (Au junctions) or ±1.2 V (Ag junctions). Positive voltage implies positive voltage on the tip. For a ± 1 V range, the sweep parameters are: 0.02 V/step, 0.02 s/step, with each trace

containing 100 points. Low-bias conductance *G* was defined as the slope of *I-V* curves within ± 0.1 V. *I-V* traces were fit to Baldea's orSLM model using fitting procedures described previously.[37,61]

Results and Discussion

Tunneling Transport and Analysis of Single Component Molecular Junctions. Single component SAMs of BOPD3, FOPD3, and OPD3 were formed and characterized on Ag^{TS} and Au^{TS} substrates; see Supporting Information for characterization information. On Au^{TS} the molecules form SAMs with thicknesses of 1.3 - 1.7 nm corresponding to molecular tilt angles on Au^{TS} of 41° for BOPD3, 29° for FOPD3 and 16° for OPD3 (see Table S1).

Typical *I-V* traces for Au^{TS}/SAM/Au^{Tip} tunnel junctions based on the single component SAMs are shown in Figure 2. Traces for Ag^{TS}/SAM/Ag^{Tip} junctions are shown in Supporting Information. We note that the conductances of the Ag junctions were significantly lower than the Au junctions, a strong indication that the facilitating orbital is the HOMO in all the systems examined here, which was subsequently verified by UPS measurements described below and in Supporting Information. The Au and Ag junction *I-V* data are well fit by Baldea's off-resonance single level model (orSLM) which is a useful simplification of the standard tunneling formula under specific assumptions that apply to the off-resonance condition, namely eV ≤ $1.3\varepsilon_h$ and $\varepsilon_h >> \Gamma$.[48,52,61] This formula for symmetric junctions reads:

$$I = GV\frac{\varepsilon_h^2}{\varepsilon_h^2-(eV/2)^2} \quad (1)$$

where

$$G = NG_0\frac{\Gamma^2}{\varepsilon_h^2} \quad (2)$$

Here G is the low bias conductance, $G_0 = 2e^2/h$ is the quantum conductance, $\Gamma = \varepsilon_h\sqrt{G/NG_0} = \sqrt{\Gamma_s\Gamma_t}$ is the *average* metal-HOMO electronic coupling to the substrate (s) and tip (t), ε_h is the

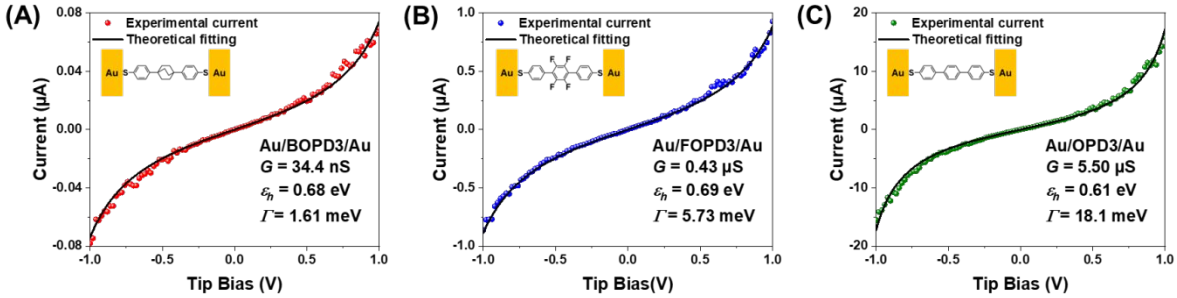

Figure 2. Current-voltage behavior of single component SAMs. Representative individual *I-V* characteristics of Au^{TS}/SAM/Au^{Tip} junctions for (A) BOPD3, (B) FOPD3, and (C) OPD3 SAMs. Black lines are two parameter fits to the off-resonance single level model (or-SLM). Fit parameters G and ε_h are shown in the insets, as well as metal-HOMO coupling Γ calculated from equation 2 using $N \cong 80$.

absolute value of the HOMO-to-Fermi level offset, and N is the number of molecules in the junction. For the ~ 25 nm^2 tip-SAM contact area, we take $N \cong 80$ molecules for the aromatic thiol junctions used here.[40]

The orSLM model has been verified for a number of junctions where the mechanism is single step, off-resonance tunneling.[39,43,44,62,63] Its utility is that it allows us to easily extract the key DOS parameters Γ and ε_h from *I-V* characteristics, as shown in Figure 2; average values and standard deviations extracted from 50-200 *I-V* curves for each type of SAM with Au or Ag contacts are listed in Table 1. It is evident in Table 1 and Figures 2a, b and c that BOPD3 junctions have the lowest conductance (G = 26 nS), followed by FOPD3 (G = 470 n S) and then OPD3 (G = 5,170 nS) with successively higher conductances. Furthermore, the extracted ε_h values are all near 0.65 eV, whereas the Γ values vary systematically and much more substantially, by more than a factor of 10: for Au junctions in Table 1, Γ = 1.4 meV for BOPD3, 5.5 meV for FOPD3, and 17.5 meV for OPD3 (see Table 1 with uncertainties). Because $G \propto \Gamma^2/\varepsilon_h^2$ (equation 2) one can immediately

see that the cause of the 150x variation in G across the molecular series is due to Γ and not ε_h. As has been well documented in other systems,[37,42,43] ε_h is effectively pinned, in this case near 0.65 eV for Au junctions and 0.75 eV for Ag junctions for all three molecules even though it can be anticipated that the molecular ionization energies vary by at least several hundred meVs.

The foregoing discussion is nicely summarized in Figure 3 for Au^{TS}/SAM/Au^{Tip} junctions. Panel A shows a comparison of the *average I-V* characteristics for all three types of SAM junctions on a semi-log plot with error bars indicating the standard deviation in the current levels obtained from 50-200 of measurements on each junction type. Panels B and C summarize the ε_h and Γ data, reinforcing the idea that ε_h is essentially pinned, whereas Γ varies by over a factor of 10 accounting for the ~150-fold difference in current levels between OPD3 and BOPD3 junctions.

Table 1. Summary of transport data for BOPD3, FOPD3, and OPD3 junctions between Au or Ag electrodes, including low-bias conductance G, HOMO-Fermi level offset ε_h, and average metal-orbital coupling Γ. Errors correspond to standard deviations for transport measurements. For UPS, the error bar is instrumental accuracy. Work function of each SAM was measured by Kelvin Probe referenced to 1-hexadecanethiol SAMs (4.3 eV) based on previous studies.[60] $\Delta\Phi$ is defined as the work function of the SAMs minus the work function of Au (5.2 eV), $\Delta\Phi = \Phi_{Au/SAM} - \Phi_{Au}$. *For OPD3 Ag junctions, the data were obtained from a previous paper.[37]

	Quantity	BOPD3	FOPD3	OPD3*
Au	G (S)	$(2.55 \pm 1.32) \times 10^{-8}$	$(4.73 \pm 1.48) \times 10^{-7}$	$(5.17 \pm 0.83) \times 10^{-6}$
	ε_h^{trans} (eV)	0.69 ± 0.05	0.68 ± 0.04	0.61 ± 0.03
	ε_h^{UPS}(eV)	0.71 ± 0.1	0.75 ± 0.1	0.69 ± 0.1
	Γ(meV)	1.37 ± 0.38	5.52 ± 1.16	17.46 ± 1.80
	Φ (eV)	5.19	5.07	4.83
	ΔΦ (meV)	-0.01	-0.13	-0.37
Ag	G (S)	$(7.65 \pm 2.57) \times 10^{-9}$	$(6.63 \pm 2.70) \times 10^{-8}$	5.34×10^{-7}
	ε_h^{trans} (eV)	0.80 ± 0.03	0.75 ± 0.03	0.73
	ε_h^{UPS}(eV)	0.85 ± 0.1	0.86 ± 0.1	0.79 ± 0.1
	Γ(meV)	0.88 ± 0.17	2.39 ± 0.55	6.82

To further verify the quality of the orSLM fit for all three junctions, we have plotted in Figure 4a all of our data for the three types of SAMs sandwiched between Au and Ag contacts, i.e., 5 types of junctions and 430 total *I-V* curves, on reduced, non-dimensional axes I_R vs V_R as defined in Supporting Information. We have presented this non-dimensional analysis previously for different tunnel junctions.[52,62] One can see that the data – which have absolute currents varying by over two orders of magnitude (see Figure 3) – collapse into a relatively narrow band of I_R-V_R traces in black. The average of these traces is shown in red. In Figure 4b we show that this average trace precisely matches the theoretical I_R vs V_R prediction for off-resonance tunneling derived from equation 1:[52,62]

$$I_R = 2V_R / \left(3 - V_R^2\right) \qquad (3)$$

In other words, the *I-V* data or BOPD3, FOPD3, and OPD3 junctions with Au or Ag contacts exhibit universal behavior consistent – in all cases considered here – with off-resonant, single level tunneling.

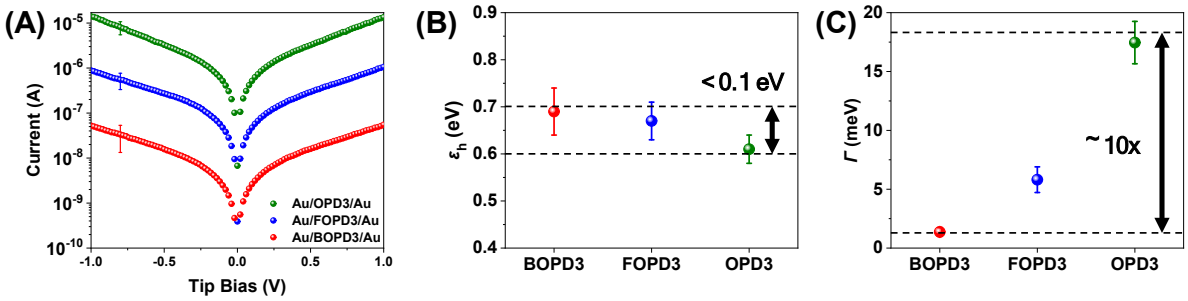

Figure 3. Comparison of average transport behavior for single component SAMs. (A) Semi-log plot of *average* *I-V* characteristics for Au^{TS}/SAM/Au^{Tip} junctions based on single component OPD3, BOPD3, and FOPD3 SAMs. (B) Average HOMO offset ε_h and (C) average Au-HOMO coupling Γ for the three types of single component junctions. Error bars represent standard deviations.

As a last check, we have measured the HOMO offset ε_h^{UPS} by UPS and have compared it to ε_h^{trans}, the offset extracted from the transport measurements for Au and Ag junctions alike,

Figure 4c and Table 1. One can see that there is excellent correspondence between ε_h^{trans} and ε_h^{UPS}, verifying the reasonableness of the ε_h^{trans} values extracted from the *I-V* curves. The fact that the ε_h^{UPS} values are systematically somewhat larger than ε_h^{trans} (they fall below the slope=1 line), is likely due to differences in image potential stabilization of the HOMO energy, as we have reported previously;[37,63] UPS measurements are necessarily made on "half junctions", i.e., there is only one metal contact, whereas transport measurements have two metal contacts. Thus, there is a small but systematic difference in measured HOMO energies due to image potential stabilization in complete junctions being roughly double that in the UPS samples.

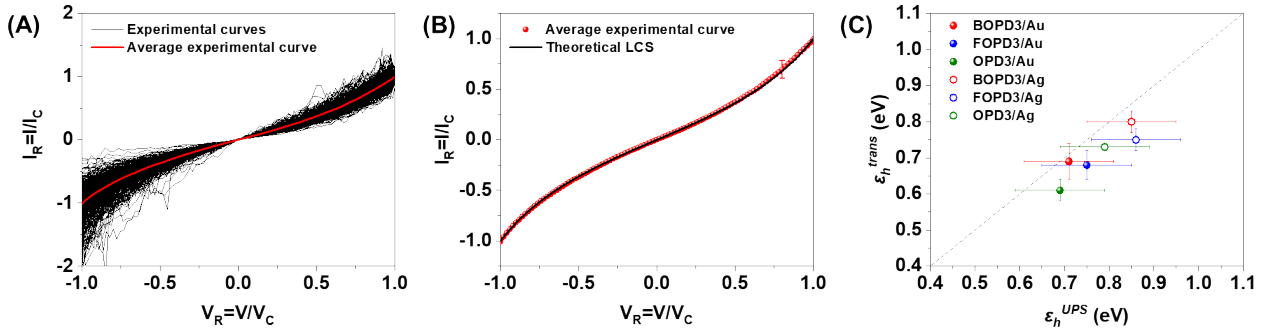

Figure 4. Verification of single-step off-resonance tunneling and universal behavior. (A) Experimental *I-V* curves (black) for 5 different junctions normalized by their critical current I_C and critical voltage V_C values. 430 *I-V* curves are represented from BOPD3, FOPD3, and OPD3 molecular junctions with Au contacts and BOPD3 and FOPD3 with Ag contacts. The absolute conductances of these 5 junction types span nearly three orders of magnitude. The average I_R-V_R curve is shown in red. See Supporting Information for the definitions of the normalizing values I_C and V_C. (B) Comparison of the theoretical I_R-V_R curve from eq. 3 and the average experimental curve shown in red. Error bar represents the standard deviation. (C) Comparison of ε_h values obtained from transport and UPS measurements for BOPD3, FOPD3, and OPD3 with Au and Ag contacts. The dashed line with slope = 1 is a guide to the eye.

Effects of Mixed SAM Composition on Tunneling Transport. With understanding of tunneling in the pure, single component SAMs in hand, we turn to the mixed systems. We prepared two types of mixed SAMs: $FOPD3_x$:$OPD3_{(1-x)}$ and $FOPD3_x$:$BOPD3_{(1-x)}$ each having varying FOPD3 fractional compositions x. Compositions in both mixtures were characterized using the normalized area of the F_{1s} core level peak in XPS scans, which was diagnostic of the mole fraction x of FOPD3

in the SAM, Figure 5. For $FOPD3_x$:$OPD3_{(1-x)}$ mixed SAMs, we found that the surface composition was directly proportional to the deposition solution concentration, Figures 5a,b. In contrast, for $FOPD3_x$:$BOPD3_{(1-x)}$ mixed SAMs, the fractional surface concentration of FOPD3 was always higher than the deposition solution fractional concentration, Figures 5c,d. It has previously been reported that the composition of mixed SAMs can differ from the deposition solution concentration, probably due to both kinetic and thermodynamic factors.[64–67] Nevertheless, for both systems we were able to systematically tune the value of x in the deposited SAMs.

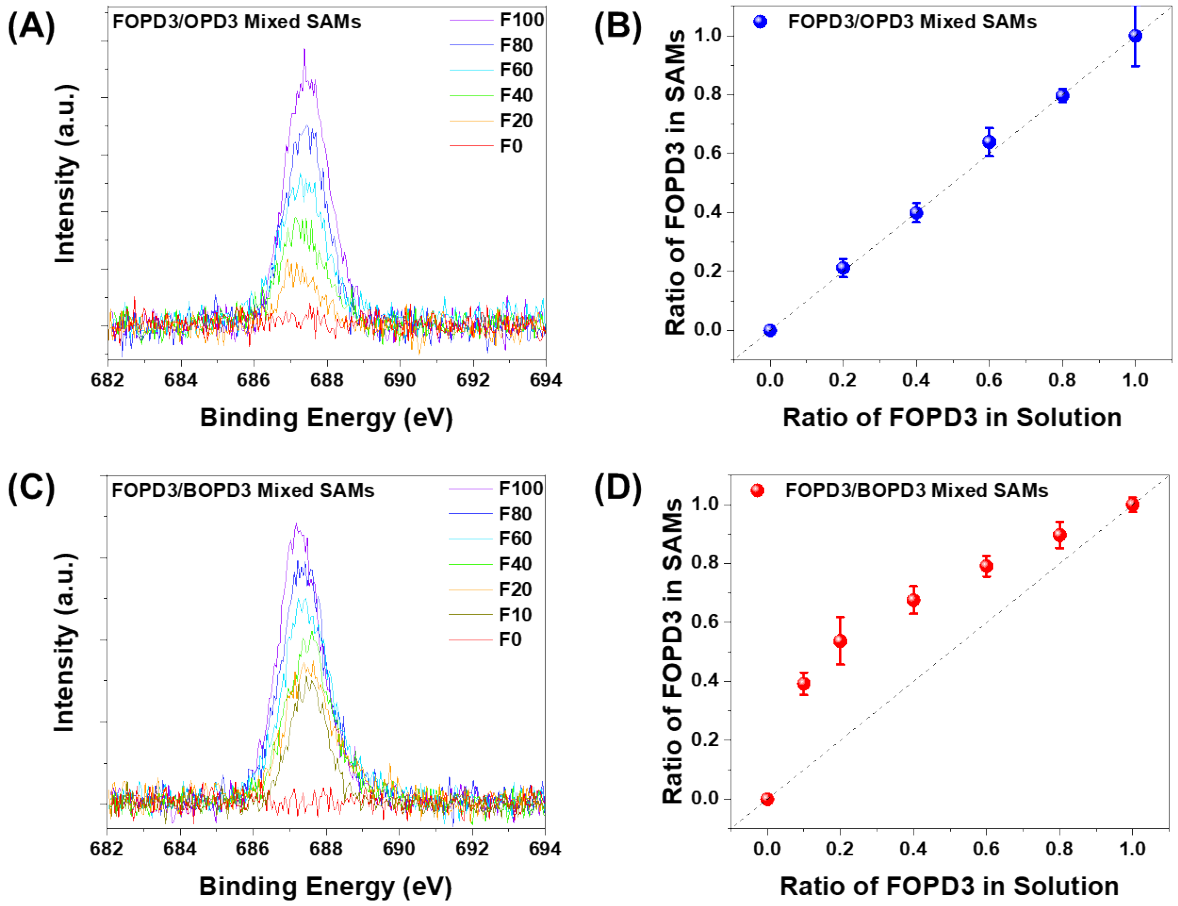

Figure 5. Formation of mixed SAMs. (A) Characterization of F_{1s} intensity for different ratios and (B) comparison of the ratio in solution versus the ratio in SAMs for $FOPD3_x$:$OPD3_{(1-x)}$ mixed SAMs. The results for $FOPD3_x$:$BOPD3_{(1-x)}$ mixed SAMs are shown in (C) and (D). The area intensities of F1s peaks were used, and they were normalized by the value of pure FOPD3 SAMs. Error bars correspond to standard deviations.

Using CP-AFM, we measured the *I-V* characteristics of Au^{TS}/ $FOPD3_x$:$OPD3_{(1-x)}$ /Au^{Tip} and Au^{TS}/ $FOPD3_x$:$BOPD3_{(1-x)}$ /Au^{Tip} junctions as shown in Supporting Information. The low bias conductance *G* of both types of junctions are displayed on a semi-logarithmic scale in Figures 6a and d. In both cases, there is a strong, exponential dependence on x, similar to what we reported for aliphatic mixed SAMs.[49] This is a somewhat surprising and interesting result, as one might have expected that the junction conductance for a mixed SAM would simply be the arithmetic mean of the two components, i.e., the sum of the *G* values for the pure component SAMs weighted by their relative coverages.

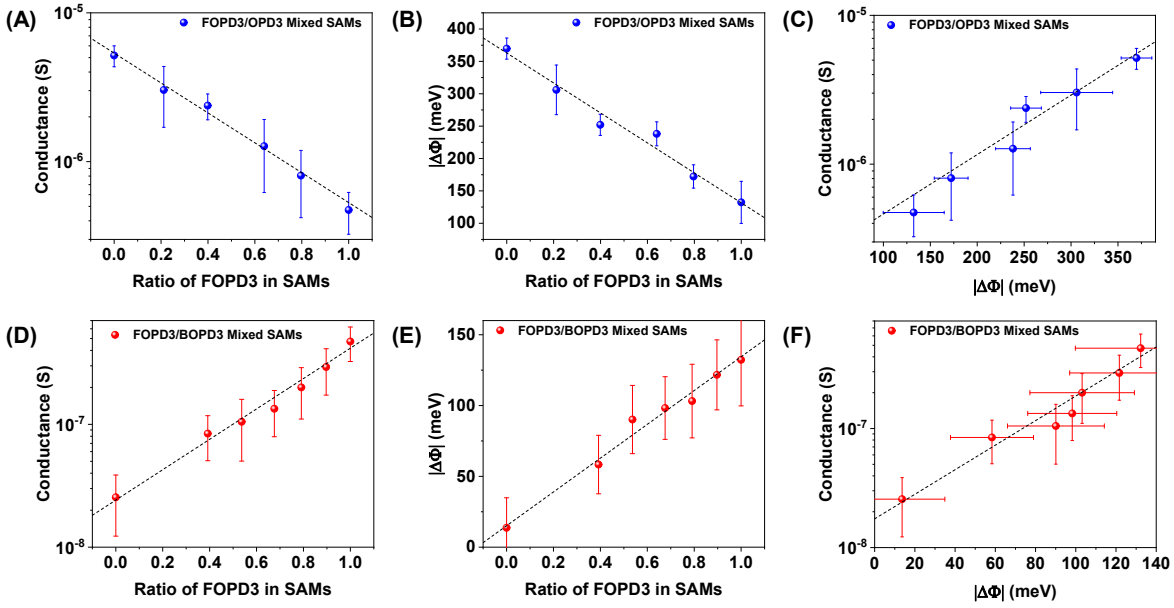

Figure 6. Conductance and work function variation with mixed SAM composition. (A) Exponential dependence of conductance on the fractional surface concentration x of FOPD3 for $FOPD3_x$:$OPD3_{(1-x)}$ mixed junctions. (B) Linear relationship between |ΔΦ| and x for $FOPD3_x$:$OPD3_{(1-x)}$, and (C) exponential dependence of conductance *G* on |ΔΦ| for $FOPD3_x$:$OPD3_{(1-x)}$. The same plots are shown in (D-F) for $FOPD3_x$:$BOPD3_{(1-x)}$ mixed junctions. Error bars represent standard deviations.

Influenced by our previous work,[39,49,50] we also measured the change in work function $\Delta\Phi = \Phi_{\text{mixed SAM}} - \Phi_{Au}$ for each mixed SAM system as a function of x using a conventional Kelvin probe. The results are shown in Figures 6b and e. In those panels it is clear that |ΔΦ|varies linearly with x for both SAM mixtures. That is, unlike *G*, |ΔΦ| can be taken to be the sum of the |ΔΦ|

values for the pure component SAMs weighted by their relative coverages. Further, as shown in Figures 6c and f, it follows that there is excellent correlation between log *G* and |ΔΦ|. This is very similar to the correlation seen for aliphatic systems.[49]

To understand this correlation in terms of the junction electronic structure, we completed an orSLM analysis of the *I-V* characteristics for both mixed SAM systems to yield ε_h^{mix} and Γ^{mix} vs x data, as shown in Supporting Information, where ε_h^{mix} and Γ^{mix} are the effective ε_h and Γ values for the mixed SAMs. It can be seen there that while ε_h^{mix} is relatively independent of composition x, Γ^{mix} is exponentially sensitive. Using the |ΔΦ| vs x data in Figures 6b,e, we present in Figure 7 our central results. Figure 7a shows all the ε_h^{mix} vs |ΔΦ| data for the two types of mixed SAMs. One can clearly see that ε_h^{mix} is relatively uncorrelated with |ΔΦ|. |ΔΦ| spans 360 meV while ε_h^{mix} changes by less than 100 meV across all 12 data points (6 for each SAM mixture). In stark contrast, Figures 7b, c, and d reveal that Γ^{mix} is exponentially correlated with |ΔΦ|. Figures 7c and 7d show Γ^{mix} vs |ΔΦ| for each of the binary SAM mixtures, respectively, where the fit lines convincingly demonstrate that the dependence is exponential across all 6 or 7 data points. Figure 7b combines the two plots in 7c and 7d so that one can better appreciate that over the 360 meV span in |ΔΦ|, with 12 separate datapoints, Γ^{mix} changed by a factor of 10. We note that trends for ε_h^{mix} and Γ^{mix} were not reported in our previous study of aliphatic systems.[49]

We take the flat ε_h^{mix} vs |ΔΦ| behavior for both mixed SAM systems to be another example of HOMO level pinning, a phenomenon that has already been extensively reported for molecular tunnel junctions.[37,42,43] For example, for single component SAM junctions based on substituted

aryl alkynes of nearly identical lengths, it has been shown that the HOMO offset ε_h is independent of molecular ionization potential, i.e., the HOMO offset in the junction is pinned.[42] We also see

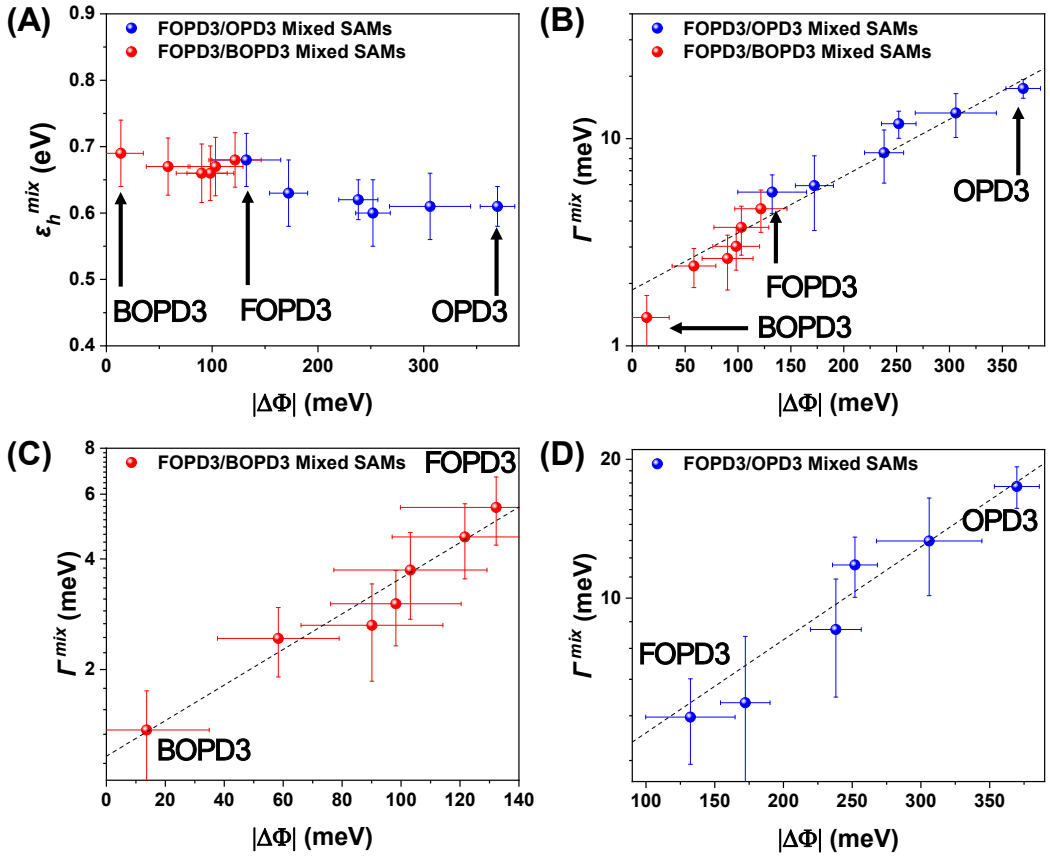

Figure 7. Junction electronic structure parameters versus change in work function. (A) ε_h^{mix} versus |ΔΦ| for $FOPD3_x$:$OPD3_{(1-x)}$ (blue) and $FOPD3_x$:$BOPD3_{(1-x)}$ (red) mixed junctions. (B) Semilog plot of Γ^{mix} versus |ΔΦ| for $FOPD3_x$:$BOPD3_{(1-x)}$ (red) and $FOPD3_x$:$OPD3_{(1-x)}$ (blue) mixed junctions. (C) Γ^{mix} versus |ΔΦ| for $FOPD3_x$:$BOPD3_{(1-x)}$ junctions only. (D) Γ^{mix} versus |ΔΦ| for $FOPD3_x$:$OPD3_{(1-x)}$ junctions only. In all cases ε_h and Γ were extracted from *I-V* characteristics using the orSLM. Note that in (A) and (B) |ΔΦ| spans 360 meV. The ε_h and Γ values for pure BOPD3, FOPD3, and OPD3 are labeled in all panels. Error bars represent standard deviations.

similar behavior in this study; the ε_h values for the single component SAM junctions based on OPD3, BOPD3, and FOPD 3 vary by only 70-80 meV, Table 1 and Figure 3b, though we can certainly anticipate much larger differences in their ionization energies. Analogously, it has also been shown repeatedly that when the molecules in the junction are kept the same and the metal contact type is changed (e.g., Ag vs Au vs Pt), the HOMO offset is also strongly pinned.[37,43] Thus, HOMO level pinning (also called Fermi level pinning when it is the metals that are varied) is

ubiquitous in MTJs. The data in Figure 7a indicate that this phenomenon also extends to mixed SAMs that have compositionally controlled work functions, thereby providing further evidence of the robustness and ubiquity of the pinning effect.

The strong exponential correlation of Γ^{mix} with $|\Delta\Phi|$ in Figures 7b-d is also reminiscent of Γ dependence on metal contact type for single component SAM junctions. It has been demonstrated that Γ can vary by over an order of magnitude for single component SAM junctions as a function of contact metal.[37,43] SAM junctions with Pt contacts, for example, have higher Γ values than junctions of the same SAMs with Au or Ag contacts, and furthermore, the Pt junctions have the biggest $\Delta\Phi$ values.[37,43] That is, there is an exponential dependence of Γ on $|\Delta\Phi|$ for single component SAM junctions. However, for any given molecular junction platform, the choice of contact metals is usually quite limited (e.g., Ag, Au, Pt, or GaIn alloy). Here, by varying the SAM composition, we have achieved an unusual degree of tunability, and we can clearly see that the strong exponential dependence of Γ^{mix} holds systematically for 12 different samples. From Figures 7b-d, we understand that strong work function dependence of Γ observed for single component SAMs also applies to mixed SAM junctions.

It is important to be clear on the meaning of Γ^{mix}. We are not suggesting that there is really only one Γ value for a given mixed junction. Because the binary mixed junctions contain two different molecules, there will be two different, composition-dependent Γ values present in each junction. However, because the CP-AFM junction samples ~80 molecules at a time, the measured *I-V* characteristics represent average behavior over this ensemble. From the good fits of the orSLM model to the mixed junction *I-V* data, we are able to extract Γ^{mix} and ε_h^{mix}, which are effective values for ε_h and Γ. Yet it is important to bear in mind that the actual electronic structure of the

junction will reflect the two populations of molecules with different composition-dependent Γ values. The same holds for ε_h, but with the key difference that ε_h^{mix} is essentially unchanging with composition x. To a good approximation, it is only the Γ values that will consist of two distinct populations in a given junction due to the two different component molecules.

Qualitatively, it seems reasonable that Γ (and Γ^{mix}) should be correlated with work function shift $|\Delta\Phi|$, as both Γ and $|\Delta\Phi|$ reflect interfacial charge transfer. Yet while the Γ vs $|\Delta\Phi|$ correlations in Figure 7 may be qualitatively rationalized, a fundamental explanation for this behavior is not at hand as far as we are aware. For that, we need a microscopic theory that can quantitatively relate metal-orbital coupling Γ to interfacial charge transfer. This theory would also need to confront the ubiquitous observation of HOMO level pinning discussed above.

We also note that Γ subsumes a number of inter-related structural and electronic factors in molecular junctions, as pointed out in the Introduction. It is well understood that bonding architecture in molecular backbones plays a crucial role in determining Γ, as does molecular length.[37,39,41,43,44] The results here on single component SAMs of OPD3, BOPD3, and FOPD3, all molecules very close to the same length, show the bonding effect quite nicely; breaking conjugation in the case of BOPD3 dramatically decreases Γ by a factor of ~10 relative to OPD3, for example. Now we must add metal-SAM work function to the list of critical parameters. Γ vs $\Delta\Phi$ behavior appears to be an important and fundamental correlation.

Conclusion

By preparing binary mixed SAMs we have examined junction transport as a function of SAM composition. We find that these mixed SAMs are well described by an analytical single level model that allows us to extract average density of states parameters for the junctions as a function

of composition. For two different mixed SAM systems, we find that ε_h is essentially independent of composition, while Γ is exponentially sensitive. Furthermore, independent measurements of metal-SAM work functions reveal that they are linearly dependent on composition. This leads to a pronounced exponential correlation of Γ with work function change $|\Delta\Phi|$; varying $|\Delta\Phi|$ by 360 meV correlates with a 10-fold change in Γ. These results reinforce and expand our previous report detailing Γ vs $|\Delta\Phi|$ correlations for alkyl thiol-based junctions, demonstrating that these correlations, now found for aromatic systems, are likely to be general. Fundamental understanding of this correlation will likely require a first principles theory, which will also need to address the cause for HOMO level pinning. For that purpose, the data presented here provide a foundation for further analysis. We note also that the results here appear to provide another good example of the utility of the analytical single level model for conveniently extracting electronic structure information from full *I-V* characteristics of simple molecular tunnel junctions.

Acknowledgements

The authors acknowledge financial support from the National Science Foundation (CHE-2304763). Portions of this work were carried out in the Minnesota Nano Center, which is supported by the National Science Foundation through the National Nanotechnology Coordinated Infrastructure (NNCI) under Award Number ECCS-2025124. Parts of this work were carried out in the Characterization Facility, University of Minnesota, which receives partial support from the National Science Foundation through the MRSEC under Award Number DMR-2011401 and the NNCI under Award Number ECCS-2025124.

References

1 T. A. Su, M. Neupane, M. L. Steigerwald, L. Venkataraman and C. Nuckolls, *Nat Rev Mater*, 2016, **1**, 16002.
2 A. Coskun, J. M. Spruell, G. Barin, W. R. Dichtel, A. H. Flood, Y. Y. Botros and J. F. Stoddart, *Chem. Soc. Rev.*, 2012, **41**, 4827.
3 B. Capozzi, J. Xia, O. Adak, E. J. Dell, Z.-F. Liu, J. C. Taylor, J. B. Neaton, L. M. Campos and L. Venkataraman, *Nature Nanotech*, 2015, **10**, 522–527.
4 H. Wang, Z. Wang, Y. Wang, J. Hihath, H.-Y. Chen, Y. Li and N. Tao, *J. Am. Chem. Soc.*, 2018, **140**, 18074–18081.
5 J. Prana, L. Kim, T. M. Czyszczon-Burton, G. Homann, S. F. Chen, Z. Miao, M. Camarasa-Gómez and M. S. Inkpen, *J. Am. Chem. Soc.*, 2024, **146**, 33265–33275.
6 S. K. Saxena, S. R. Smith, M. Supur and R. L. McCreery, *Advanced Optical Materials*, 2019, **7**, 1901053.
7 W. Peng, N. Chen, C. Wang, Y. Xie, S. Qiu, S. Li, L. Zhang and Y. Li, *Angew Chem Int Ed*, 2023, **62**, e202307733.
8 S. Soni, I. Werner, M. Aidi, M. Moors, C. L. Mthembu, M. Zharnikov, R. W. A. Havenith, K. Yu. Monakhov and R. C. Chiechi, *ACS Appl. Nano Mater.*, 2023, **6**, 22643–22650.
9 A. M. Najarian and R. L. McCreery, *ACS Nano*, 2019, **13**, 867–877.
10 H. B. Li, Y.-F. Xi, Z.-W. Hong, J. Yu, X.-X. Li, W.-X. Liu, L. Domulevicz, S. Jin, X.-S. Zhou and J. Hihath, *ACS Sens.*, 2021, **6**, 565–572.
11 X. Wang, T. L. R. Bennett, A. Ismael, L. A. Wilkinson, J. Hamill, A. J. P. White, I. M. Grace, O. V. Kolosov, T. Albrecht, B. J. Robinson, N. J. Long, L. F. Cohen and C. J. Lambert, *J. Am. Chem. Soc.*, 2020, **142**, 8555–8560.
12 W.-Y. Lo, W. Bi, L. Li, I. H. Jung and L. Yu, *Nano Lett.*, 2015, **15**, 958–962.
13 J. Park, L. Belding, L. Yuan, M. P. S. Mousavi, S. E. Root, H. J. Yoon and G. M. Whitesides, *J. Am. Chem. Soc.*, 2021, **143**, 2156–2163.
14 J. Park, M. S. Kodaimati, L. Belding, S. E. Root, G. C. Schatz and G. M. Whitesides, *ACS Nano*, 2022, **16**, 4206–4216.
15 Y. Liu, S. Katzbach, A. Asyuda, S. Das, A. Terfort and M. Zharnikov, *Phys. Chem. Chem. Phys.*, 2022, **24**, 27693–27704.
16 T. M. Czyszczon-Burton, E. Montes, J. Prana, S. Lazar, N. Rotthowe, S. F. Chen, H. Vázquez and M. S. Inkpen, *J. Am. Chem. Soc.*, 2024, jacs.4c11241.
17 S. Kumar, M. Merelli, W. Danowski, P. Rudolf, B. L. Feringa and R. C. Chiechi, *Advanced Materials*, 2019, **31**, 1807831.
18 I. Hnid, A. Yassin, I. Arbouch, D. Guérin, C. Van Dyck, L. Sanguinet, S. Lenfant, J. Cornil, P. Blanchard and D. Vuillaume, *Nano Lett.*, 2024, **24**, 2553–2560.
19 S. Guo, J. Hihath, I. Díez-Pérez and N. Tao, *J. Am. Chem. Soc.*, 2011, **133**, 19189–19197.
20 C. Bruot, J. Hihath and N. Tao, *Nature Nanotech*, 2012, **7**, 35–40.
21 Z. Miao, T. Quainoo, T. M. Czyszczon-Burton, N. Rotthowe, J. M. Parr, Z.-F. Liu and M. S. Inkpen, *Nano Lett.*, 2022, **22**, 8331–8338.
22 X. Chen, M. Roemer, L. Yuan, W. Du, D. Thompson, E. Del Barco and C. A. Nijhuis, *Nature Nanotech*, 2017, **12**, 797–803.
23 T. Abu-Husein, S. Schuster, D. A. Egger, M. Kind, T. Santowski, A. Wiesner, R. Chiechi, E. Zojer, A. Terfort and M. Zharnikov, *Adv Funct Materials*, 2015, **25**, 3943–3957.
24 A. Nitzan and M. A. Ratner, *Science*, 2003, **300**, 1384–1389.
25 M. Thoss and F. Evers, *The Journal of Chemical Physics*, 2018, **148**, 030901.

26 J. Koo, Y. Jang, L. Martin, D. Kim, H. Jeong, K. Kang, W. Lee, J. Kim, W.-T. Hwang, D. Xiang, E. Scheer, M. Kabdulov, T. Huhn, F. Pauly and T. Lee, *ACS Appl. Mater. Interfaces*, 2019, **11**, 11645–11653.

27 H. Reddy, K. Wang, Z. Kudyshev, L. Zhu, S. Yan, A. Vezzoli, S. J. Higgins, V. Gavini, A. Boltasseva, P. Reddy, V. M. Shalaev and E. Meyhofer, *Science*, 2020, **369**, 423–426.

28 S. Fujii, T. Tada, Y. Komoto, T. Osuga, T. Murase, M. Fujita and M. Kiguchi, *J. Am. Chem. Soc.*, 2015, **137**, 5939–5947.

29 C. Jia, A. Migliore, N. Xin, S. Huang, J. Wang, Q. Yang, S. Wang, H. Chen, D. Wang, B. Feng, Z. Liu, G. Zhang, D.-H. Qu, H. Tian, M. A. Ratner, H. Q. Xu, A. Nitzan and X. Guo, *Science*, 2016, **352**, 1443–1445.

30 Y. Isshiki, T. Nishino and S. Fujii, *J. Phys. Chem. C*, 2021, **125**, 3472–3479.

31 Y. Zang, A. Pinkard, Z.-F. Liu, J. B. Neaton, M. L. Steigerwald, X. Roy and L. Venkataraman, *J. Am. Chem. Soc.*, 2017, **139**, 14845–14848.

32 X. Li, Y. Zheng, Y. Zhou, Z. Zhu, J. Wu, W. Ge, Y. Zhang, Y. Ye, L. Chen, J. Shi, J. Liu, J. Bai, Z. Liu and W. Hong, *J. Am. Chem. Soc.*, 2023, **145**, 21679–21686.

33 Y. Han, C. Nickle, Z. Zhang, H. P. A. G. Astier, T. J. Duffin, D. Qi, Z. Wang, E. Del Barco, D. Thompson and C. A. Nijhuis, *Nat. Mater.*, 2020, **19**, 843–848.

34 W. Du, X. Chen, T. Wang, Q. Lin and C. A. Nijhuis, *J. Am. Chem. Soc.*, 2024, **146**, 21642–21650.

35 E. J. Dell, B. Capozzi, J. Xia, L. Venkataraman and L. M. Campos, *Nature Chem*, 2015, **7**, 209–214.

36 C. M. Bowers, K.-C. Liao, T. Zaba, D. Rappoport, M. Baghbanzadeh, B. Breiten, A. Krzykawska, P. Cyganik and G. M. Whitesides, *ACS Nano*, 2015, **9**, 1471–1477.

37 Z. Xie, I. Bâldea and C. D. Frisbie, *J. Am. Chem. Soc.*, 2019, **141**, 3670–3681.

38 H. Wang, F. Hu, A. Adijiang, R. Emusani, J. Zhang, Q. Hu, X. Guo, T. Lee, L. Chen and D. Xiang, *J. Am. Chem. Soc.*, 2024, jacs.4c13773.

39 Z. Xie, I. Bâldea, C. E. Smith, Y. Wu and C. D. Frisbie, *ACS Nano*, 2015, **9**, 8022–8036.

40 Z. Xie, I. Bâldea, A. T. Demissie, C. E. Smith, Y. Wu, G. Haugstad and C. D. Frisbie, *J. Am. Chem. Soc.*, 2017, **139**, 5696–5699.

41 C. E. Smith, Z. Xie, I. Bâldea and C. D. Frisbie, *Nanoscale*, 2018, **10**, 964–975.

42 S. Rodriguez-Gonzalez, Z. Xie, O. Galangau, P. Selvanathan, L. Norel, C. Van Dyck, K. Costuas, C. D. Frisbie, S. Rigaut and J. Cornil, *J. Phys. Chem. Lett.*, 2018, **9**, 2394–2403.

43 Z. Xie, I. Bâldea and C. D. Frisbie, *J. Am. Chem. Soc.*, 2019, **141**, 18182–18192.

44 Q. V. Nguyen, Z. Xie and C. D. Frisbie, *J. Phys. Chem. C*, 2021, **125**, 4292–4298.

45 K. Kanthasamy, M. Ring, D. Nettelroth, C. Tegenkamp, H. Butenschön, F. Pauly and H. Pfnür, *Small*, 2016, **12**, 4849–4856.

46 A. Kovalchuk, T. Abu-Husein, D. Fracasso, D. A. Egger, E. Zojer, M. Zharnikov, A. Terfort and R. C. Chiechi, *Chem. Sci.*, 2016, **7**, 781–787.

47 A. R. Garrigues, L. Wang, E. Del Barco and C. A. Nijhuis, *Nat Commun*, 2016, **7**, 11595.

48 I. Bâldea, *Phys. Chem. Chem. Phys.*, 2024, **26**, 6540–6556.

49 J. Feng, I. Bâldea, J. Gao, G. Jeong, C. D. Frisbie and Z. Xie, *ACS Nano*, 2024, **18**, 32016–32022.

50 B. Kim, S. H. Choi, X.-Y. Zhu and C. D. Frisbie, *J. Am. Chem. Soc.*, 2011, **133**, 19864–19877.

51 V. B. Engelkes, J. M. Beebe and C. D. Frisbie, *J. Am. Chem. Soc.*, 2004, **126**, 14287–14296.

52 I. Bâldea, Z. Xie and C. D. Frisbie, *Nanoscale*, 2015, **7**, 10465–10471.

53 G. T. Paganoto, M. L. A. Temperini and D. P. Dos Santos, *J. Phys. Chem. C*, 2024, **128**, 15974–15984.

54 S. Tao, Q. Zhang, C. He, X. Lin, R. Xie, C. Zhao, C. Zhao, A. Smogunov, Y. J. Dappe, R. J. Nichols and L. Yang, *ACS Appl. Nano Mater.*, 2019, **2**, 12–18.

55 C. A. Nijhuis, W. F. Reus and G. M. Whitesides, *J. Am. Chem. Soc.*, 2009, **131**, 17814–17827.

56 Z. Xie, I. Bâldea, G. Haugstad and C. Daniel Frisbie, *J. Am. Chem. Soc.*, 2019, **141**, 497–504.

57 Y. Wang, Q. Zhang, H. P. A. G. Astier, C. Nickle, S. Soni, F. A. Alami, A. Borrini, Z. Zhang, C. Honnigfort, B. Braunschweig, A. Leoncini, D.-C. Qi, Y. Han, E. Del Barco, D. Thompson and C. A. Nijhuis, *Nat. Mater.*, 2022, **21**, 1403–1411.

58 A. N. Parikh, D. L. Allara, I. B. Azouz and F. Rondelez, *J. Phys. Chem.*, 1994, **98**, 7577–7590.
59 S. Karpe, M. Oçafrain, K. Smaali, S. Lenfant, D. Vuillaume, P. Blanchard and J. Roncali, *Chem. Commun.*, 2010, **46**, 3657.
60 A. Asyuda, X. Wan and M. Zharnikov, *Phys. Chem. Chem. Phys.*, 2020, **22**, 10957–10967.
61 I. Bâldea, *Phys. Rev. B*, 2012, **85**, 035442.
62 Z. Xie, I. Bâldea, S. Oram, C. E. Smith and C. D. Frisbie, *ACS Nano*, 2017, **11**, 569–578.
63 Z. Xie, V. Diez Cabanes, Q. Van Nguyen, S. Rodriguez-Gonzalez, L. Norel, O. Galangau, S. Rigaut, J. Cornil and C. D. Frisbie, *ACS Appl. Mater. Interfaces*, 2021, **13**, 56404–56412.
64 P. E. Laibinis, M. A. Fox, J. P. Folkers and G. M. Whitesides, *Langmuir*, 1991, **7**, 3167–3173.
65 P. E. Laibinis, R. G. Nuzzo and G. M. Whitesides, *J. Phys. Chem.*, 1992, **96**, 5097–5105.
66 J. P. Folkers, P. E. Laibinis, G. M. Whitesides and J. Deutch, *J. Phys. Chem.*, 1994, **98**, 563–571.
67 T. Yu, M. D. Marquez and T. R. Lee, *Langmuir*, 2022, **38**, 13488–13496.

Data Availability Statement

for

Molecular Tunnel Junctions Based on Mixed SAMs: Exponential Correlation of the Average Metal-HOMO Coupling with SAM/Metal Work Function

Gookyeong Jeong, C. Daniel Frisbie*

Department of Chemical Engineering and Materials Science, University of Minnesota, Minneapolis, Minnesota 55455, United States

*E-mail: frisbie@umn.edu

The data supporting the findings of this study are included in the article and SI. Additional raw data can be obtained from the corresponding author upon request.